This is an open access article published under an ACS AuthorChoice License, which permits copying and redistribution of the article or any adaptations for non-commercial purposes.

ACS NANO

www.acsnano.org

ARTICLE

Chiral Graphene Quantum Dots

Nozomu Suzuki,[†,‡,§] Yichun Wang,[‡,⊥] Paolo Elvati,[⊥,∥] Zhi-Bei Qu,[†] Kyoungwon Kim,[†,‡] Shuang Jiang,[†] Elizabeth Baumeister,[∥] Jaewook Lee,[‡,¶,○] Bongjun Yeom,[†,‡,□] Joong Hwan Bahng,[‡,⊥] Jaebeom Lee,[¶] Angela Violi,*[,⊥,∥,△] and Nicholas A. Kotov*[,‡,⊥,∥,#]

[†]Department of Chemical Engineering, [‡]Biointerfaces Institute, [⊥]Department of Biomedical Engineering, [∥]Department of Mechanical Engineering, [#]Department of Materials Science and Engineering, and [△]Department of Macromolecular Science and Engineering, Biophysics Program, University of Michigan, Ann Arbor, Michigan 48109, United States

[§]Graduate School of Materials Science, Nara Institute of Science and Technology, Ikoma, Nara 8916-5, Japan

[¶]Department of Cogno-Mechatronics Engineering, Pusan National University, Miryang 627-706, Republic of Korea

Supporting Information

ABSTRACT: **Chiral nanostructures from metals and semiconductors attract wide interest as components for polarization-enabled optoelectronic devices. Similarly to other fields of nanotechnology, graphene-based materials can greatly enrich physical and chemical phenomena associated with optical and electronic properties of chiral nanostructures and facilitate their applications in biology as well as other areas. Here, we report that covalent attachment of L/D-cysteine moieties to the edges of graphene quantum dots (GQDs) leads to their helical buckling due to chiral interactions at the "crowded" edges. Circular dichroism (CD) spectra of the GQDs revealed bands at *ca.* 210−220 and 250−265 nm that changed their signs for different chirality of the cysteine edge ligands. The high-energy chiroptical peaks at 210−220 nm correspond to the hybridized molecular orbitals involving the chiral center of amino acids and atoms of graphene edges. Diverse experimental and modeling data, including density functional theory calculations of CD spectra with probabilistic distribution of GQD isomers, indicate that the band at 250−265 nm originates from the three-dimensional twisting of the graphene sheet and can be attributed to the chiral excitonic transitions. The positive and negative low-energy CD bands correspond to the left and right helicity of GQDs, respectively. Exposure of liver HepG2 cells to L/D-GQDs reveals their general biocompatibility and a noticeable difference in the toxicity of the stereoisomers. Molecular dynamics simulations demonstrated that D-GQDs have a stronger tendency to accumulate within the cellular membrane than L-GQDs. Emergence of nanoscale chirality in GQDs decorated with biomolecules is expected to be a general stereochemical phenomenon for flexible sheets of nanomaterials.**

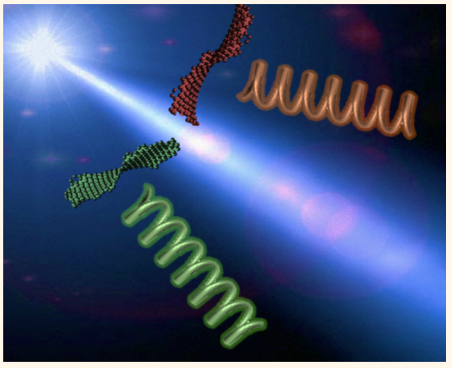

KEYWORDS: *chirality, graphene quantum dots, circular dichroism, chiral excitons, biological activity*

Chirality of inorganic nanostructures found in individual inorganic nanoparticles and their assemblies have attracted increasing attention over the past decade.[1−7] Unusually high intensity of chiroptical phenomena due to plasmonic and excitonic effects characteristic of nanoscale materials fuels this interest.[3−6,8,9] Necessity of further development of this field is incentivized by technological prospects for chiral nanostructures associated with negative refractive materials,[10] hyperbolic metasurfaces,[11] high-sensitivity bioanalysis,[3,9,12] and chiral catalysis.[13] The palette of chiral geometries obtained for inorganic nanostructures is broad, but the variety of inorganic materials and organic components used for their construction is not. The chiral nanostructures are being made predominantly from gold due to spectral convenience of its plasmonic bands, chemical stability, and exciting physics.[6,9,14−17] The studies of chiral semiconductor nanostructures[18−20] are less frequent due to weaker polarization rotation, but in return, they reveal distinctive chiroptical effects due to higher chemical activity.[8,18,21]

Research on different forms of nanoscale carbon[22−27] is abundant and, by some measures, exceeds in volume the research on nanoscale forms of gold. The synthesis of chiral nanocarbons is mostly focused on chirality at the atomic scale and represents a well-known chemical problem and is difficult to translate from other areas of asymmetric synthesis. For instance, the methods suitable for the synthesis of chiral fullerenes[28] cannot be extended to the preparation of enantiopure carbon nanotubes (CNTs) because the growth of the graphene network requires a temperature in the range of several hundred degrees on the Celsius scale, but traditional asymmetric catalysts cannot survive it.[25,26,29,30] Synthesis[31,32]

Received: October 9, 2015
Accepted: January 8, 2016
Published: January 8, 2016

Downloaded via HANYANG UNIV on July 29, 2021 at 05:37:04 (UTC).
See https://pubs.acs.org/sharingguidelines for options on how to legitimately share published articles.

© 2016 American Chemical Society

DOI: 10.1021/acsnano.5b06369
ACS Nano 2016, 10, 1744−1755

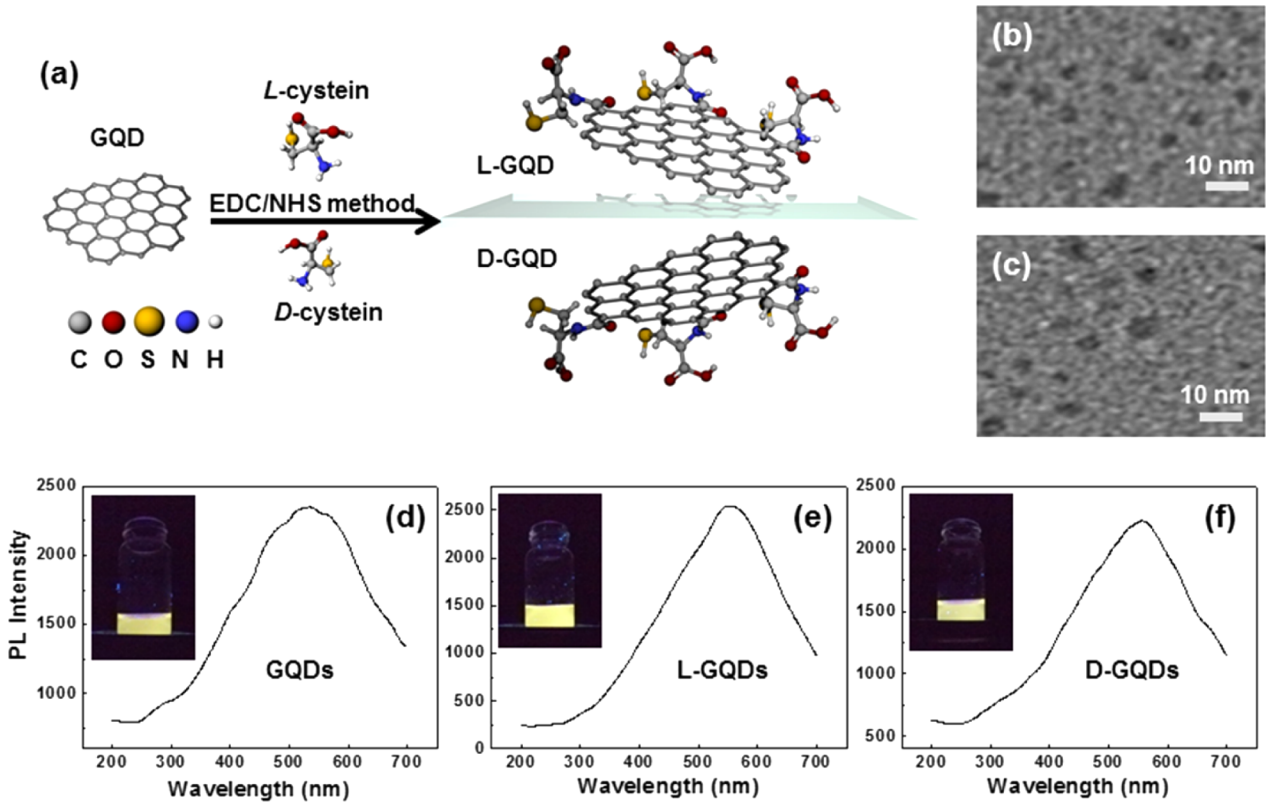

Figure 1. (a) Molecular schematics of chiral GQD synthesis. Only a portion of the graphene sheet of GQD is shown. (b,c) TEM images of (b) L-GQD and (c) D-GQD dispersions. (d–f) Photoluminescence spectra of (d) pristine, (e) L-GQD, and (f) D-GQD dispersions under ambient conditions. Insets of (d–f): photographs of the corresponding dispersions being illuminated by UV light with λ_{max} = 365 nm.

and separation[33,34] of CNTs with chiral conformation of graphene sheets is possible and symmetry-matched nanotubes with opposite rotatory optical activity have recently become available.[35,36] Particularly interesting would be to obtain chiral forms of graphene, but chiral nanocarbons based on graphene are virtually unknown. Chirality of graphene nanoribbons was found only for singular pieces with the help of atom probe microscopy.[37]

The need for comparative evaluation of carbon nanostructures in symmetrically paired (*i.e.*, mirror image) forms and understanding different manifestation of their chirality would be essential for many fields of science: quasiparticle physics,[38] optics,[39] electronics,[37] drug delivery,[40] and biomedical imaging.[41] Graphene quantum dots (GQDs) represent the basic and most recent forms of nanocarbon relevant for all of these areas.[42−45] Additionally, exciton confinement in GQDs[44] and plasmonic effects in graphene sheets[46,47] make this nanoscale material similar to both noble metal and semiconductor nanostructures. Studies of chiral GQDs will be essential for understanding chiroptical phenomena in delocalized states and their utilization in biology and medicine, which motivated us to synthesize symmetrically paired GQDs in dispersions. Based on the previous studies,[21] we hypothesized that chiral GQDs and potentially other forms of graphene sheets with nanoscale chirality can be obtained due to intermolecular interactions of chiral surface ligands[48] leading to out-of-plane buckling of the graphene sheets (Figure S1).

RESULTS AND DISCUSSION

Synthesis and Structural Characterization. The hypothesis of asymmetric synthesis of GQDs was tested starting from aqueous dispersions. Most of the work reported below used GQD dispersions made according to Peng *et al.*[49] unless otherwise stated. Successful formation of a GQD dispersion with characteristic bright yellow photoluminescence (PL, Figure 1) and a size of 2−7 nm was observed. L-Cysteine or D-cysteine moieties were covalently bound to the edges of the carbon sheets using carbodiimide/*N*-hydroxysuccinimide (EDC/NHS) cross-linking protocol;[50] the corresponding products are denoted here as L- and D-GQDs (Figure 1a). Note that L- and D-GQD notations refer here to the synthetic route and molecular chirality of the amino acid incorporated in the product. The reason for this choice of the notations rather than others exemplified by *R*/*S*, *M*/*P*, or Δ/Λ notations often used in case of chiral macromolecules and supramolecular assemblies, is that prior to the use of these notations we have to identify the geometry of GQDs and the origin of chiroptical properties, which is the goal of this study. The chiral symmetry and handedness of the GQDs will be discussed later based on the established 3D geometry of the graphene sheets.

TEM images show that GQDs before and after modification have similar sizes in the 2−7 nm range, with fairly broad size distribution expected of GQDs (Figure 1b,c).[49] Atomic force microscopy images confirm the size range of GQDs and their polydispersity (Figure S2). Due to the nanoscale dimensions of this form of nanoscale carbon, the XRD peak at $2\theta = 25°$ is broad; it can be attributed to (002) carbon-to-carbon spacing of 3.7 Å. The XRD peak is similar for all forms of GQDs and remains unchanged before and after modification (Figure S3).

Small graphene sheets with a few nanometers in diameter are known to exhibit quantum confinement.[42,44,51,52] The UV−visible absorption spectrum of pristine GQDs reveals a peak at

DOI: 10.1021/acsnano.5b06369
ACS Nano 2016, 10, 1744−1755

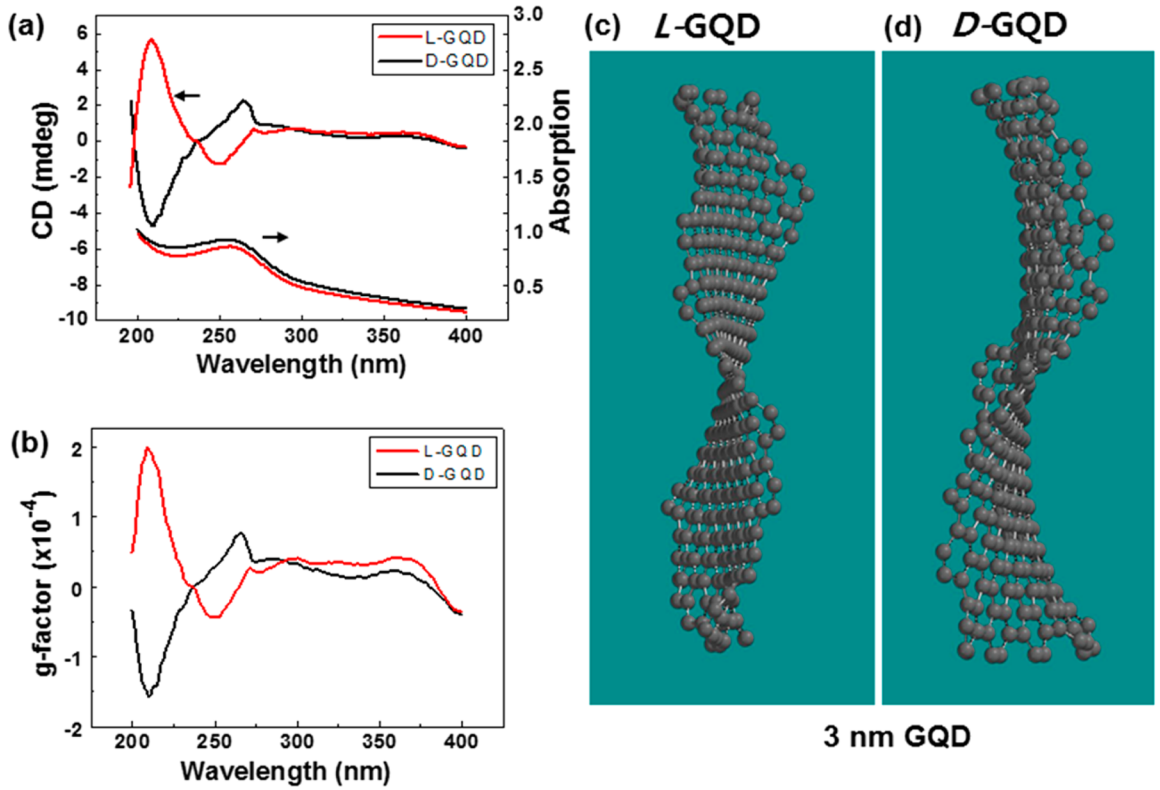

Figure 2. (a,b) Circular dichroism (a) and *g*-factor (b) spectra for L-GQD (red) and D-GQD (black) dispersions. (c,d) Optimized geometry of a graphene sheet in model GQDs viewed from the direction of the largest dihedral angle, θ. Note that the handedness (*i.e.*, rotatory direction) of helices is opposite to the handedness of the edge ligands. The chirality of the ligands is noted on the top of the image; they were removed for clarity.

228 nm, which is strongly blue-shifted compared to that of graphene or carbon nanotubes.[53] The UV−vis absorption peak of L/D-GQDs is observed at 265 nm (Figure 2) and indicates partial relaxation of exciton confinement due to the hybridization of the aromatic system of the graphene dot with the atomic orbitals on cysteine moieties. Concomitant spectral changes also develop in PL spectra. Being excited by photons with λ_{ex} = 330 nm, pristine, L-, and D-forms of GQDs all display strong emission at 520−550 nm (Figure 1d−f). The red shift after the modification with the amino acid in the PL peaks is, nonetheless, subtle (Figure 1d−f). Comparison with the absorption spectra of both pristine and cysteine-modified graphene dots in Figure 2 reveals strong Stokes shift of the synthesized GQDs. The reason for the large energy difference between the first absorption band with lowest energy at 260−270 nm and emission band at 520−550 nm can be formation of small agglomerates in which GQDs of different sizes are likely to be present. In this case, emission should occur from the particles with lowest energy, as was observed for semiconductor quantum dots.[54,55] Formation of exciplex states known for the red shift of the emission of anthracene, coronene, and other aromatic hydrocarbons is also possible.[56]

The electrokinetic zeta-potential (ζ) of pristine GQDs is −26.7 mV (Figure S4a). After attachment of cysteine moieties, ζ-potentials of L- and D-form chiral GQDs become −12.7 mV (Figure S3b) and −10.3 mV (Figure S3c), respectively, which is consistent with amidation of negatively charged −COOH groups at GQD edges while retaining a substantial degree of ionization.

The entirety of spectroscopy and microscopy data points to the conjugation of cysteine moieties to the edges of the graphene sheets, which can be further affirmed by both Fourier transform infrared (FT-IR) and Raman spectroscopy. FT-IR spectra of pristine, L-, and D-GQDs show the presence of the carbonyl, carboxyl, hydroxyl, and epoxy groups (Figure S5a). The vibrational signatures of O−H bonds can be found at 3400 cm^{-1}, C−H bonds (aliphatic stretching mode) at 2960 cm^{-1}, C=C bonds (skeletal vibrations of non-oxidized graphitic domains aromatic group) at 1620 cm^{-1}, C−H at 1420 cm^{-1}, and alkoxy C−O bonds at 1170 cm^{-1}.[57] After conjugation with cysteine, new peaks appeared at 2390 and 930 cm^{-1} from S−H and C−N bonds, respectively. The former one originates from attached cysteine ligands, while the latter one indicates covalent bonding between the carbon of GQD and the amino group of cysteine (Figure 1a). Assignment of the FT-IR peaks was further substantiated by the calculations of vibrational spectra using Merck molecular force field (MMFF) developed for evaluation of conformations of drugs: all the peaks in the fingerprint region of 800−1800 cm^{-1} match those observed experimentally (Figure S5b).

Raman spectroscopy was used to elucidate the chemical state of the graphene network of the GQDs (Figure S6a). The original and modified GQDs display A_{1g} D band at 1355 cm^{-1} and E_{2g} G band at 1590 cm^{-1}.[58,59] The weak ∼2700 cm^{-1} peak corresponding to a 2D harmonic band can be found in all samples. The relative intensities I_D/I_G are close to 1.0, which is higher than that for GQDs prepared by electrochemical etching (I_D/I_G = 0.5).[60] Most importantly, the positions and relative intensities in Raman scattering peaks do not change after the modification with cysteine, indicating intactness of the central graphene sheets. Importantly, GQDs also display distinct enhancement of Raman bands of crystal violet molecules.[61]

DOI: 10.1021/acsnano.5b06369
ACS Nano 2016, 10, 1744−1755

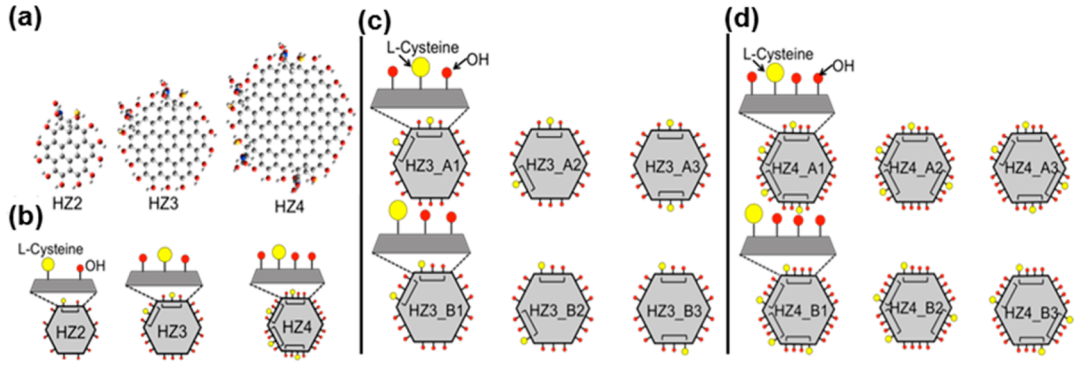

Figure 3. (a–d) Molecular models of L-GQDs of different sizes and placements of L-cysteine edge ligands used in the computational evaluation of their geometry and optical properties.

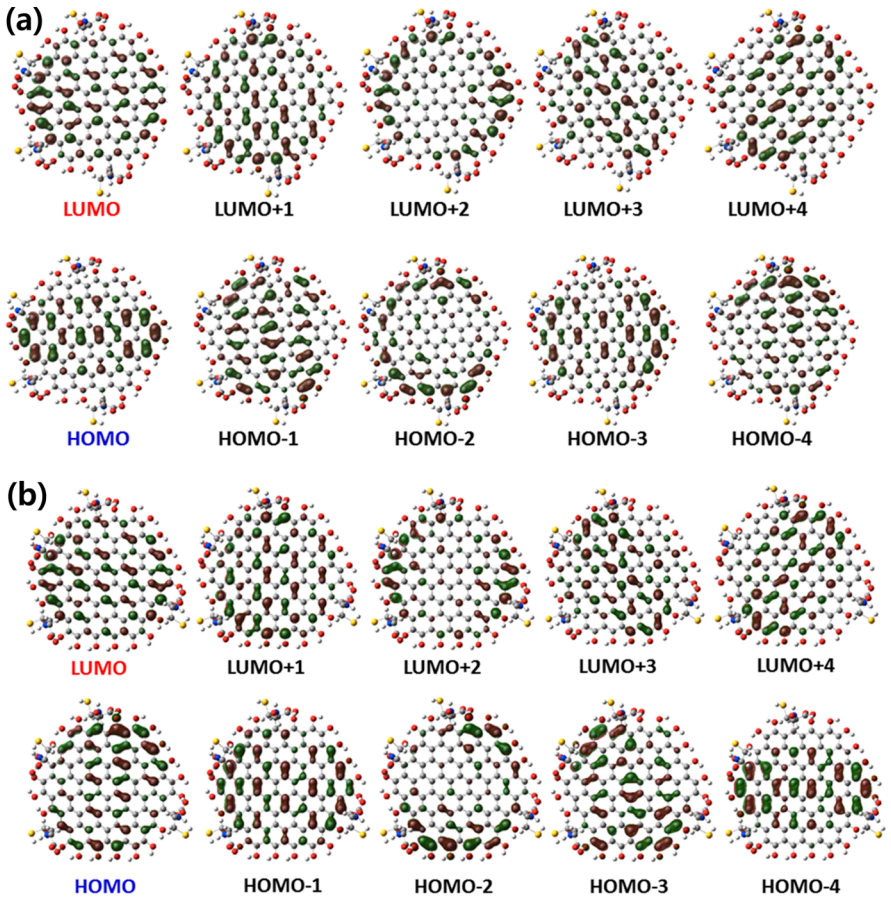

Figure 4. Molecular orbitals for HZ4 GQDs exemplified by (a) HZ4–A1 and (b) HZ4–A2 regioisomers. Additional MO calculations for HZ3 and HZ2 are given in the Supporting Information.

This typical surface-enhanced Raman scattering (SERS) label was incorporated between the graphene dots following the standard process using aqueous solution.[62] The sharp intense SERS lines of crystal violet matching those obtained for gold particles[61–64] indicate that the synthesized GQDs exhibit some properties characteristic of plasmonic particles.

Chiroptical Properties of L/D-GQDs. The ring-like arrangement of chiral ligands in GQDs is conducive to the asymmetric preference in the conformation of the entire "molecule" due to collective chiral interactions of the chiral ligands known for many supramolecular assemblies and macromolecules.[65–67] Chiroptical activity of L- and D-GQDs indicative of the preference toward a specific stereoisomer can be observed in CD spectra (Figure 2). The high-energy peak at 210–220 nm matches that in the CD spectra of free cysteine at 209 nm (Figure S7).[68] Both L- and D-GQDs concomitantly gave rise to a new peak at 250–265 nm (Figure 2a). Importantly, this new low-energy chiroptical band has opposite signs depending on the chirality of the amino acid used for conjugation to the GQDs, whereas the graphene sheets (Figure S8a), unmodified GQDs (Figure S8b), and *rac*-GQDs (*i.e.*, made with racemic mixture of L- and D-cysteine, Figure S8c) display no chiroptical activity in CD spectra at 250–265 nm. The asymmetry of the CD peaks in respect to the abscissa (*i.e.* imperfect mirror-image spectra) was reproducible in several independent synthetic series carried out by two experimental

DOI: 10.1021/acsnano.5b06369
ACS Nano 2016, 10, 1744–1755

materials chemists (K.K. and Z.-B.Q.), who performed these experiments 2 years apart. The low-energy peak for D-GQDs was always red-shifted compared with that for L-GQDs. Such asymmetries are not uncommon in the studies of chiral supramolecules and in case of GQDs are likely to reflect variable contributions of different isomer sizes of sheets and GQD agglomerates present in L- and D-dispersions. At the present stage of research in this area, it is difficult to speculate about its origin and should be the subject of a dedicated study.

The chiroptical asymmetry parameter also known as the *g*-factor of chiral GQDs at the 250−265 nm chiroptical band is equal to 1×10^{-4} and comparable to that of many chiral organic compounds (Figure 2b) but lower than for many chiroplasmonic assemblies.[3,4,9,12,69] No circularly polarized luminescence was observed at room temperature for both types of GQDs despite multiple conditions tested.

The low-energy CD band at 250−265 nm is of particular interest because it overlaps with the UV−vis absorption peak at 260 nm (Figure 2a,c), corresponding to the band gap of GQDs. Its origin can be associated with a variety of molecular and nanoscale geometries,[14,70−72] which is difficult to establish using only experimental methods. Computational tools can be particularly helpful in this task, complementing the spectroscopic and microscopy data. Moreover, when carrying out quantum mechanical and other computations of GQDs, one will benefit from well-established interaction potentials for atoms frequently encountered in organic chemistry and biology that make calculations of equilibrium geometry of GQDs easier than for semiconductor or metal NPs.

Emergence of chiroptical activity at wavelengths longer than those of cysteine ligands can be attributed, among other possibilities, to perturbation of electronic states of the graphene segment by the ligands and change of the conformational structure of the chromophore itself. It is conceivable that the molecular orbitals (MOs) of chiral edge ligands exert the symmetry-breaking perturbation to electronic states of graphene. We evaluated the hypothesis of symmetry perturbation (also known as chirality induction) by calculating MOs of GQD's using the semiempirical ZINDO algorithm for three sizes of L-GQDs with two, three, and four rings of carbon atoms denoted as HZ2, HZ3, and HZ4 (Figures 3, 4, and S9−S11), respectively. These GQD sizes are realistic for quantum mechanical methods, while large sizes are possible for less computationally intense techniques exemplified by MMFF. In accord with the previously discussed experimental data in Figures S3−S8, L-cysteine ligands were added to the edges of the graphene sheets *via* amide bonds. Their number took into account the data from XPS spectroscopy using a sulfur−carbon atomic ratio (Table S1).

HZ2 GQDs reveal distinct hybridization between atomic orbitals (AOs) of the graphene sheet and the edge ligands, for example, for LUMO+2 and LUMO+4 (Figure S9). Similar electronic levels produced by combining AOs of graphene and cysteine can be found for LUMO+3 in HZ3_A1 GQD, but the extent of mixing is much lower; in other regioisomers represented by HZ3_A3, one cannot find hybridized MOs even for high-level LUMOs and HOMOs (Figures S10 and S11). HZ4-type GQDs do not show the presence of MO made from AOs of cysteine and graphene up to LUMO+4 and HOMO−4.

Heuristic expectations for the hybridization of AOs from graphene sheets and covalently attached functional groups based on general MO theory match these calculations: the hybridization of the chiral electronic states of the edge ligand is more likely to occur for smaller GQDs. As GQD becomes larger, the difference in energies between the electronic states of L/D-cysteine and the graphene sheet becomes wider. Importantly, HZ4-type GQDs are smaller than the lower size threshold in 2−7 nm GQD dispersions. As an illustration, 5 nm GQDs contain about 10 circles of aromatic rings. Thus, one would not expect the hybridized orbitals to form for our GQDs at the MO energies corresponding to the 250−265 nm CD band.

We also considered the possibility that chiroptical bands originate not from the chirality induction by the ligands in the entire GQD but only in a small segment of the graphene sheet. For instance, the cysteine ligand can be attached to a benzene ring or a double −C═C− bond that does not have strong electron delocalization with the rest of the graphene sheet. It can occur in a variety of chemical structures at the GQD edges that also sustained partial oxidation/reduction (Figure S12). Such a mechanism can be described as local chirality induction. We calculated UV−vis and CD spectra for HZ2 versions where L-cysteine is covalently bonded to localized benzene, ethane, or carbonyl groups (Figure S12). Indeed, for several of them, the *in silico* spectra show similarities with the experimental ones, such as the presence of the two UV−vis absorption peaks from cysteine and from graphene segments; they also display a negative chiroptical band at 250 nm, attributed to MOs localized at the edges of GQDs. With the exception of the low intensity of CD and UV absorption peaks at 210 nm corresponding to cysteine, the combination of two types of GQDs with cysteine ligands bonded to a localized benzene ring gives spectra that resemble experimental ones (Figure S14).

Diverse chemistry of the GQD edges makes it possible that the localized chiral MOs obtained by hybridization of AOs of cysteine and graphene segments with partial breakage of sheet aromaticity may indeed be responsible for chiroptical activity of L/D-GQDs. If this is true, the relatively large GQDs with a diameter of 10−15 nm produced commercially must also display the same band. However, no CD or UV−vis bands could be identified above 220 nm for a variety of L/D-GQDs concentrations (Figure S15). Although localized MOs may be responsible for some effects, they are unlikely to play the central role in the genesis of the 250−265 nm CD band as well as other chiroptical bands at longer wavelengths.

Emergence of chiroptical properties of L/D-GQDs can also be associated with the overall shape of this molecule. As the first level for *in silico* evaluation of molecular geometries of GQD, we used the same MMFF algorithm used for calculating the IR spectrum (Figure S5). MMFF assumes nearly elastic deformation of covalent bonds and can be a powerful tool for understanding complex mechanics of large molecules. It is also computationally much less demanding than density functional theory (DFT) and semiempirical ZINDO algorithms, and thus, many large atomic systems matching the median size of our basic 2−7 nm GQD could be calculated with the MMFF algorithm.

As expected, the equilibrium geometries of small unmodified GQDs display nearly perfect molecular flatness (Figure S16). Angstrom-scale "ripples" appear at the edges of the graphene sheets as the diameter of the sheets becomes bigger, indicating the tendency of these structures to relieve some strain from atomic repulsion by buckling deformations. When, L-cysteine ligands were added around the circumference of GQD, an increase of buckling deformation was observed. In fact, the

DOI: 10.1021/acsnano.5b06369
ACS Nano 2016, 10, 1744−1755

equilibrium geometry of these GQDs displayed a strong twist; GQDs carrying L-cysteine and D-cysteine revealed right- and left-handed twists of the GQD, respectively (Figure 2c). The enhancement of buckling is attributed to noncovalent intermolecular interactions of the ligands with each other and other edge groups. Intermolecular chiral interactions at the periphery of the large molecules are known to cause molecular deformation and translate the nanoscale chirality in liquid crystals, polymers, proteins, and dendrons.[66,73−75]

Their mirror images of twisted graphene sheets are not superimposable and therefore should lead to the appearance of the characteristic chiroptical band(s). The closest symmetry point group describing their geometry would be D_2 as they tend to have two perpendicular C_2 rotational axes. The twisted graphene sheets can also be characterized as axial chiral structures, and thus, L- and D-GQDs can also be denoted as *P*- and *M*-GQDs or alternatively as Δ- and Λ-GQDs. The *R*/*S* notation is not applicable here because of ambiguity of the Cahn−Ingold−Prelog ranking for "substituents" in the GQD case, unlike the case of tetrahedral NP assemblies[76] or NPs with tetrahedral chiral centers in the apexes[70] reported before. The electronic transition responsible for the 250−265 nm band can be attributed to promotion of the electron and hole to one of the excitonic states of GQDs and can be referred to as chiral excitonic transition.

An important point needs to be made that many of the twisted molecular geometries are dynamic and can flex into the symmetrically opposite conformation if the energy barrier between these conformational states is lower than kT, which is the essential difference with large-scale supramolecular chiral systems. This energy barrier between different twisted conformations is dependent, among other factors, on the bending modulus of the graphene sheet of the size of starting GQDs. Since linear mechanics was found to be generally applicable to graphene sheets,[77] one can conclude that the larger the sheets, the smaller their buckling modulus is.[78,79] A lower-energy threshold for transition of one buckled state to another leads to the more dynamic twisted state. Eventually, GQDs of large diameter must exist as a racemic mixture, combining both left- and right-handed twisted sheets in equal amounts regardless of the chirality of the edge ligands because the threshold of racemization becomes smaller than kT. Therefore, for 10−15 nm L/D-GQDs in Figure S15, the CD band at 250−265 nm disappears. Instead, the CD bands in the 180−230 nm window characteristic of cysteine showed distinct broadening that should be attributed to chiral induction based on mixing MOs from edge ligands and graphene discussed above.

MMFF can be versatile, fast, and accessible to many researchers, but it cannot be applied to calculation of optical properties. Taking into account the twist of GQDs, we calculated the CD and UV−vis absorption spectra using DFT +ZINDO algorithms, although these computational tools restricted us to GQDs of smaller sizes presented in Figure 3 rather than those in Figure 2c,d.

In the first venue of these calculations, we optimized GQD conformation for a variety of GQD sizes and regioisomers. The computational results obtained in the first venue tested the possibility of spontaneous twisting of GQDs. In the second venue, we preset the dihedral angle of the base graphene sheets of GQD, θ, to have certain values and then calculated CD spectra of twisted GQDs. The data obtained in the second venue provided detailed understanding of the influence of dihedral angle on chiroptical properties.

The primary question that we wanted to answer here is whether the presence of dihedral angle θ may account for the emergence of the (low-energy) 250−265 nm band and resolve the discrepancies discussed above. We largely ignored the high-energy states associated with cysteine and related molecular edge segments considered above because the origin of 210−220 nm CD bands in L/D-GQDs caused little doubts. We also need to point out the limitation of computational methods we applied in this study. ZINDO is known to deviate the energy of electronic transitions.[80] So, it is difficult to expect the perfect match in the spectral location of all the experimental and calculated CD bands, and we were not able to obtain it except for those associated with hybridized MO at the edges of GQDs. However, the relative energies of transitions for different GQD sizes can be properly compared. The sign of the calculated CD bands and the Cotton effect are the parameters that we can use as the first level of "yes/no" discrimination when comparing experimental results.

DFT calculations confirmed that the twisted conformation of L-GQDs (Figure 2c,d) represents the equilibrium geometry. Spontaneous buckling results in complex shapes with multiple nonzero dihedral angles (Figure S1), and the chiroptical properties of the particle will be determined by their superposition. To obtain a representative set of *in silico* data, we considered the possibility of incomplete and/or inhomogeneous modification of the graphene edge, and multiple regioisomers of GQDs with different placements of cysteine moieties were considered and calculated (A1−3 and B1−3 isomers, Figure 3b−d) in recognition of the polydispersity of the molecular structure of GQDs. Therefore, we calculated the chiroptical activity of all of the variants and regioisomers of L-GQDs. Some of them have positive and some of them have negative Cotton effects (Figure S12a,b). The calculations of a collective rotatory activity of the GQD dispersion representing many conformations must, therefore, take into account the statistical probability of ligand placement and intensity of the rotatory activity. Hence the cumulative CD spectra were calculated as a superposition of statistically weighted contributions from different isomers in Figure S16. The sign of the Cotton effects and the first low-energy "wave" in the cumulative calculated CD spectra in Figure S18 matched the experimental ones in Figure 2. The blue shift of the UV−vis and CD signatures with reduction of the GQD size (Figure 3e) coincided with the expectations about the excitonic state of GQDs being responsible for their rotatory activity. One could also see that in the computational spectra for HZ2-type GQDs, the complexity of CD bands increases due to increasing contribution of hybridized MOs. The overall intensity of the chiroptical bands decreases in the order HZ4 > HZ3 > HZ2 due to reduced optical cross section of the GQD molecules.

In the second venue of calculations, we constructed five atomistic models of HZ4 with preset dihedral angles θ = 0, +5, +10, +15 and +20° while allowing the GQDs under this boundary condition to optimize its atomic structure. CD spectra were calculated using the ZINDO algorithm and IEFPCM. We found that UV−vis spectra of GQDs were not affected by different values of θ, but the CD spectra were affected to a large extent (Figure 5). The rotatory activity consistently increases, and the CD spectrum becomes ever more complex as θ increases. A parallel can be made with the significance of the twist angle in other chiral molecular and

DOI: 10.1021/acsnano.5b06369
ACS Nano 2016, 10, 1744−1755

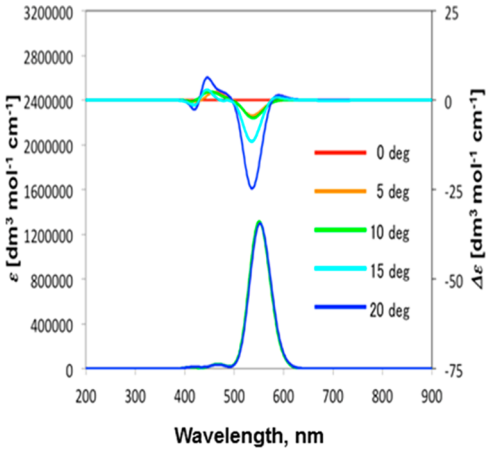

Figure 5. CD spectra of HZ4 L-GQDs calculated using the second DFT venue (see Methods). All the spectra were calculated as angle-averaged functions to reflect random orientation of L-GQDs with respect to the incident light beam in dispersions. In all spectra, mostly the electronic states corresponding to the graphene sheet, *i.e.*, the first 20 states, were calculated.

nanoscale chemical structures exemplified by a family of axial compounds based on 1,1′-binaphthyl[81] or DNA-bridged plasmonic assemblies from gold nanorods/nanoparticles.[82,83]

Similarly to proteins and some drugs, chiral nanostructures may exhibit different biological activity depending on their handedness.[84] Unlike CdTe and other heavy-metal-based NPs, the cytotoxicity originating from NP components will not interfere in this case with the biological activity of the stereoisomer. So, we tested how L/D-GQDs affect the viability of human liver hepatocellular carcinoma cells HepG2 that represent a common model for cytotoxicity studies. Extensive investigation for different times of exposure, concentrations, and cell numbers confirmed that biocompatibility of GQDs is high (Figures S19–S21). The negative effect on cells compared to the control group is insignificant after 1 h of exposure (Figure S19). It becomes discernible only after 24 h of incubation in the presence of GQDs (Figure S20) and results in a decrease of HepG2 cell viability by *ca.* 20% for all concentrations of GQDs used: 0.015, 0.03, and 0.045 mg/mL. The difference in toxicity between L- and D-GQDs is small. For the two highest concentrations of GQDs (*i.e.*, 0.045 or

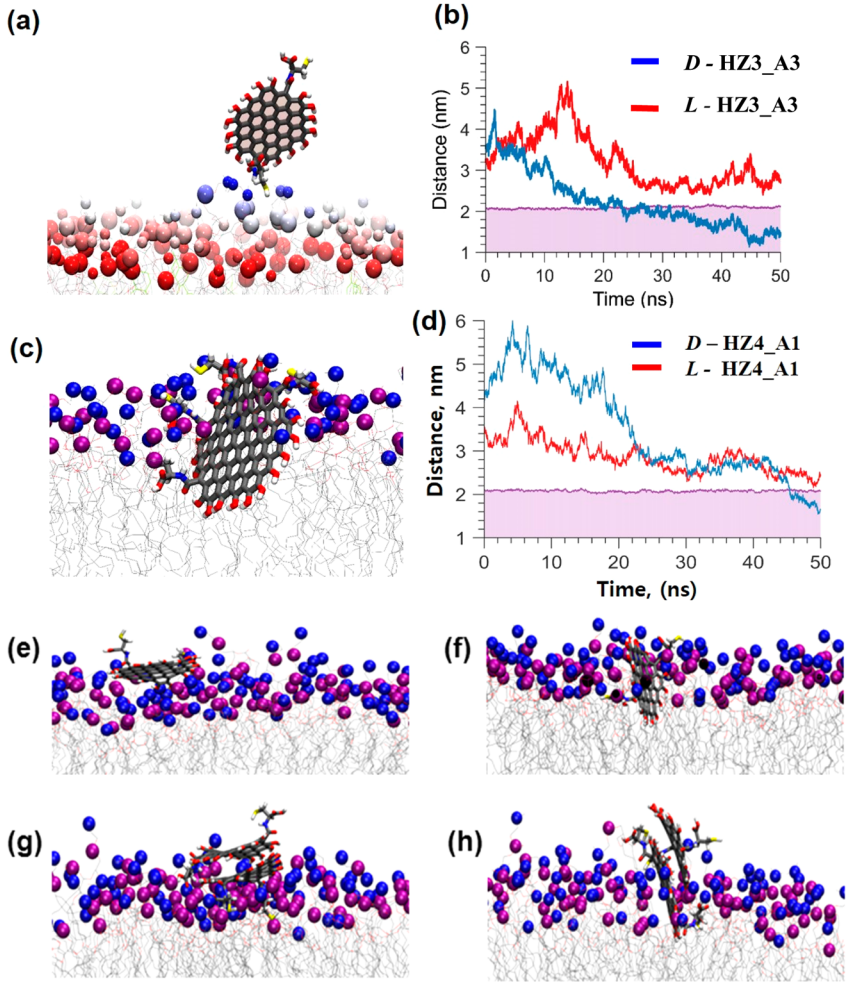

Figure 6. (a,c) Snapshots from the atomistic MD simulations of a variant of HZ3_A3 D-GQD (a) and HZ4_A1 D-GQD (c) in the vicinity of the cellular membranes. The chemical groups on the membrane surface are extended toward the GQD. (b,d) Time dependences of the distances from GQD to the center of the bilayer (projection on the axis normal to the bilayer plane) for HZ3_A3 D-GQD (b) and HZ4_A1 (d). Background colors show the regions of the water (white) and the membrane (light purple). (e–h) Snapshots of GQD/membrane interactions near the completion point of the simulations. Blue and purple spheres represent the position of phosphoric and nitrogen atoms of POPC, respectively, while the gray thin lines show the rest of the lipids' structure.

DOI: 10.1021/acsnano.5b06369
ACS Nano 2016, 10, 1744–1755

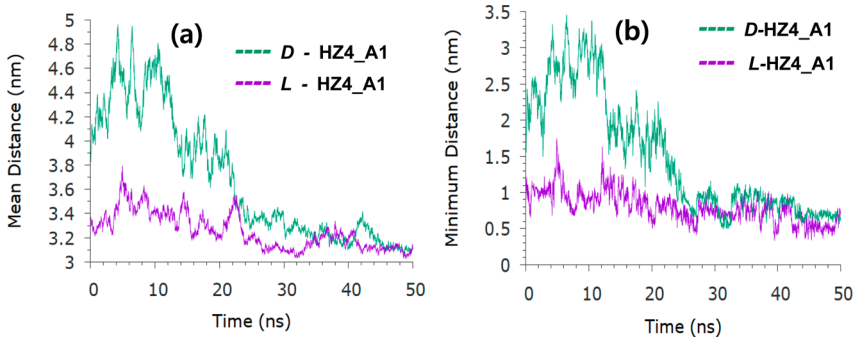

Figure 7. Time dependence of the (a) mean and (b) minimum distances between any of the chiral carbons of the HZ4_A1 GQD and any of the chiral carbons of the POPCs.

0.030 mg/mL of GQDs), it becomes statistically significant and can be observed for 25 000−100 000−25 000 cells per well (Figures S19 and S20). Notably, L-GQDs show slightly higher overall biocompatibility than D-GQDs (Figures S19 and 20). The similar relationship between L- and D-enantiomers can be seen for free cysteine in our experiments (Figure S21) as well as other studies on chirality effects for the toxicity of drugs and drug candidates.[85−87] It is perhaps instructive to point out that no free amino acid was present in the dialysis-purified dispersions of L- and D-GQDs used in experimental series described in Figures S19−S21.

There can be multiple biological pathways for how the chirality of GQDs and cysteine can affect cellular functions. To our surprise, the mechanism of toxicity differentiation between enantiomers is poorly understood even for free L/D-cysteine. In the case of L- and D-GQDs, the difference in biological effects can be even more complicated than for free amino acids because it can be related to both atomic chirality of the edge ligands and the nanoscale chirality of the twisted graphene sheets. Previous studies of adhesion of neuronal[88] and mesenchymal bone marrow[89] cells on L/D-cysteine-modified surfaces indicate that interactions with cellular membranes are likely to play the central role in differentiation between the two isomers. The intermolecular forces causing the difference in association with biological membranes and, thus, in toxicity between L- and D-GQDs are hydrogen bonds by van der Waals interactions and interactions with hydrophobic forces. It is essential to note that at the scale of a few nanometers these interactions become nonadditive,[90] and thus, the traditional distinction between the forces becomes ambiguous. Atomistic molecular dynamics (MD) studies become one of the best ways to elucidate them, although limitations of the current atomistic potentials should also be taken into account.

Interactions of the GQD stereoisomer with cellular membranes were evaluated using advanced MD simulations where both GQD and a bilayer lipid membrane composed of 1-palmitoyl-2-oleoyl-*sn*-glycero-3-phosphocholine (POPC) and cholesterol was described at an atomistic level using the CHARMM force field[91] with particle mesh Ewald method[92] to evaluate long-range forces. The simulations were carried out in six different systems: two systems with a single D/L-GQD of HZ3_A3-type (Figure 6a,b,e,f), two systems with a single D/L-GQD of HZ4_A1-type (Figure 6c,d), and two with a stack of identical GQDs of HZ3_A3-type and to reflect the possibility of agglomeration (Figure 6g,h). The evidence of possible agglomeration can be seen in the large Stokes shift between the first excitonic transition of GQDs at 260 nm and the maximum of photoluminescence at *ca.* 530 nm (Figure 2).

During all the MD runs, all GQDs remained less than 1 nm away from the membrane surface with the cysteine ligands bent toward the membrane. This observation is indicative of strong intermolecular interactions between GQD and membrane lipids *via* hydrogen bonding and van der Waals forces. When near the surface, the single D-GQD both for HZ3_A3 and HZ4_A1 cases markedly disturbed the structure of the bilayer, as some lipids extended in the water toward the GQD (Figure 6a,c). After about 15 ns, the D-GQD with HZ3_A3 structure entered the head group region of the membrane, while the surface structure was slowly restored (Figure 6b). Incorporation into the membrane was also observed for D-GQD with HZ4_A1 structure, although this process was about 3 times slower due to the higher molecular mass of the larger GQD (Figure 6d). In all cases, the graphene (aromatic) part of the GQDs lay perpendicularly to the bilayer plane, with the two amino acids surrounded by the phosphate and choline groups of the POPC lipid head groups in the membrane.

After different orientational states were explored in half-inserted position, D-GQD slowly moved in the glycerol region of the lipids (Figure 6a−d) and eventually penetrated deep into the lipid bilayer (Figure S22). Conversely, L-GQDs never entered the bilayer. Such lack of affinity between the L-GQDs and the external part of the cellular membrane was observed for both HZ3 and HZ4 GQDs (Figure 6b,d). To rule out simple coincidence, we repeated this simulation five times, placing the GQD at different distances and angles with respect to the membrane. In all cases, the L-GQD stayed parallel to the bilayer at less than 1 nm from the surface (Figure 6b,d). We can speculate that the difference in association with the membranes between L- and D-GQDs is determined in the case of small HZ3-type and HZ4-type quantum dots by the edge groups because the nanoscale twist for small graphene sheets is not yet pronounced as it is for larger GQDs (see above). The contribution of the nanoscale twist is, at the moment, uncertain and will require further MD study evaluating the behavior of the system at much longer times, which presents multiple fundamental and hardware limitations.

Considering stronger toxicity differentiation between the stereoisomer at higher concentrations of L- and D-GQDs (Supporting Information, Figures S13 and S14), we analyzed the behavior of a pair of stacked GQDs having the same chirality. The GQDs were prepared in a "closed stack" configuration that is likely to be formed in dispersions as their concentration increases.[93] L-GQD and D-GQD stacks showed that they remained intact for the duration of the whole simulation. Overall, the behavior of agglomerates is similar to that of single GQDs. D-GQD stacks quickly entered in the

DOI: 10.1021/acsnano.5b06369
ACS Nano 2016, 10, 1744−1755

bilayer and remained halfway inserted, with the aromatic plane laying normal to the membrane for the rest of the simulation (Figure 6g). On the other hand, L-GQD stacks stayed near the surface but remained parallel to it, never leaving the water region above the bilayer (Figure 6h). Considering the intermolecular forces that could lead to such a difference of behavior between aggregates of L- and D-GQDs, it is essential to point out that the carbon dots explored the full range of angles even when they were 3 nm away from the bilayer center (Figure S22). The mean and minimal distances between the chiral centers of GQDs and those of POPC in the membrane model indicate that L-GQDs tend to stay closer to the contact with the chiral center of the lipid than do D-GQDs (Figure 7). This may suggest that intermolecular interactions between L-GQDs and the lipid layer are favorable to the parallel orientation of the graphene sheet and the membrane. Such a configuration makes entering the bilayer more difficult for L-GQDs than for D-GQDs.

CONCLUSIONS

In this study, we described the asymmetric synthesis of chiral GQDs by covalent edge modification with L- and D-cysteine, leading to the nanoscale twist of the flexible graphene sheets. Quantum mechanical chiral induction occurs at the edges of the GQDs due to hybridization of MOs of the the edge-ligands and those of peripheral carbon atoms. Resulting L- and D-GQDs represent an example of symmetry-related carbon nanostructures with nearly mirror image optical activity. L-GQDs and D-GQDs reveal a 210−220 nm CD peak corresponding to the amino acid broadened by hybridization with edge groups of the graphene sheets. GQDs also display a new chiroptical band at 250−265 nm that is associated with the twisted excitonic state of the graphene sheet. The twist in the graphene sheet originates from collective interactions of amino acid moieties bound to the graphene base *via* amide bonds. While multiple regioisomers and conformations are possible for cysteine-modified GQDs, atomistic simulations using multiple methods indicate that L-GQDs preferentially display right helicity in their twisted state whereas D-GQDs have predominantly left-handed conformation. Therefore, L- and D-GQDs can also be identified as *P*- and *M*-GQDs, respectively, following the notations for helical structures with clockwise and counterclockwise rotations. Strong luminescence and SERS activity point to the possibility of circular polarization effects in both photoluminescence[94] and Raman scattering[95] that need to be investigated further.

In vitro evaluation of GQD biocompatibility with liver cells demonstrated their low cytotoxicity and differentiation of cytotoxicity between GQD stereoisomers. Atomistic simulations of L- and D-GQDs interacting with cellular membranes demonstrated stronger binding of D-GQDs to the lipid bilayer of the cells.

Biocompatibility of chiral GQDs opens new routes for development of drug delivery vehicles and more selective phototherapies, while the twisted electronic states can lead to polarization-based optoelectronic devices and (photo)catalysts.

METHODS

Materials and GQD Synthesis. The carbon fiber was obtained from Fiber Glast Development Co. (Brookville, OH). L/D-Cysteine, sulfuric acid, nitric acid, and *N*-ethyl-*N*′-(dimethylaminopropyl)-carbodiimide (EDC, 191.7 g/mol) were purchased from Sigma-Aldrich and Thermo Scientific. *N*-Hydroxysuccinimide (NHS, 115.09 g/mol) was purchased from Thermo Scientific. The GQDs were synthesized by a modified protocol from a previous report.[49] Through a top-down process, 0.5 g of carbon fibers was dispersed into a 40 mL mixture of sulfuric acid and nitric acid (3:1 v/v). The black solution was sonicated for 2 h and mechanically stirred for one additional day at 80 °C. After the reaction, the mixture solution was cooled and diluted with DI water (0.15 mg/mL). To adjust to pH 8, sodium hydroxide was added into the solution. For purification of GQDs, the mixture was dialyzed for 3 days. Large GQDs with diameters exceeding 15 nm were obtained from Sigma-Aldrich.

Synthesis of Chiral GQD. Synthesis of chiral GQDs was carried out at room temperature using L/D-cysteine. In order to impart chirality to the GQDs, the carboxylic group of GQDs was connected with the amine group of L-(or D-)cysteine by the EDC/NHS method. A solution of EDC (30 μL, 6 mM) was added into 0.5 mL of GQD solution. After 10 min stirring, the same amount of NHS (6 mM) was added to the solution and it was mixed for 30 min. Finally, 30 μL of L-(or D-)cysteine (6 mM) was added into the graphene GQD-NHS, and the mixture was stirred for 30 min. The surplus L/D-form of cysteine was removed by a dialysis membrane (Viskase, Membra-cell MD 34).

Surface-Enhanced Raman Scattering Measurements. Crystal violet (Fisher) was used without further purification; its 1×10^{-6} M solution in water was mixed with isovolumetric L/D-GQDs. Approximately, 20 μL of this solution was deposited on clean silicon wafers and dried. Raman spectra were recorded using a Witec microscope with a 100× Zeiss objective. A 532 nm continuous-wave laser light was used for excitation of the Raman scattering with a spectral collection time of 1 s for all of the measurements.

Instrumentation. The chiroptical activity of the dispersions was measured by CD spectroscopy (JASCO, J-815), and the chemical reaction progress was monitored by FT-IR spectroscopy (Nicolet 6700) and Raman spectroscopy (Witec, Alpha 300 D, USA). The absorbance of chiral GQD was analyzed by UV/vis spectroscopy (Agilent, 89090A). The fluorescence property of chiral GQDs was characterized by PL spectroscopy (Horiba, Fluoromax-3). The morphology of chiral GQDs was observed by HR-TEM (JEOL, JEM-3011). Their surface potential was analyzed by a Zetasizer (Malvern Instruments, Nano ZS).

DFT Quantum Mechanical Studies of the GQD Conformers. Conformation search was carried out using the CONFLEX method (searching limit = 3.0 kcal/mol) with MMFF94S as a force field. After the search, the most stable conformation of each structure was chosen for each configuration (first venue) or each structure with preset $\theta = 0$, +5, +10, +15, and +20° (second venue). DFT calculation at the B3LYP/6-31G(d) level with IEFPCM (solvent = water) level was carried out followed by ZINDO calculation to obtain the CD spectrum. Generalized Born/solvent-accessible surface (GB/SA) model (solvent = water) was used for GQDs with L-cysteine (first venue). For GQDs with preset θ (second venue), the twisted forms were maintained during the CONFLEX search as well as DFT calculation (see Supporting Information for further description). These calculations can be carried out only for L-GQD because geometry optimization by CONFLEX used a deterministic rather than a stochastic algorithm; it has to yield mirror inversion of equilibrium geometry.

Cell Cultures. Hepatocellular carcinoma human cells (HepG2) (ATCC, VA) were maintained with Eagle's minimum essential medium (EMEM) supplemented with 10% fetal bovine serum (FBS) and 1% penicillin−streptomycin (ATCC) in a humidified incubator (MCO-15AC, Sanyo) at 37 °C in which the CO_2 level was maintained at 5% before seeding. All of the medium was filtered using 0.22 μ SteriCup filter assembly (Millipore, USA) and stored at 4 °C for no longer than 2 weeks. For cells incubated with the L-form, D-form, and control GQDs, the cells were cultured overnight to allow attachment in a 96-well plate, washed with FBS-free EMEM, and then incubated with L-GQDs, D-GQDs, and control GQDs with a concentration of 0.015 mg/mL at 37 °C for 1 h in FBS-free medium. After incubation with GQD, the cells were washed repeatedly with sterilized PBS and maintained in culture medium before further analysis.

DOI: 10.1021/acsnano.5b06369
ACS Nano 2016, 10, 1744−1755

Cell Viability Assays. PrestoBlue cell viability reagent (Life Technologies) was used to measure cell viability. In brief, HepG2 cells were seeded into a 96-well flat culture plate (Corning). After being cultured overnight, the cells were washed with FBS-free EMEM and incubated with a specific concentration of L-GQD and D-GQD in FBS-free medium at 37 °C for 1 h. The cells were then washed three times with sterilized PBS and incubated with fresh medium containing 10% FBS overnight. The cells were then washed with PBS, and FBS-free EMEM (500 mL) was used to substitute the culture medium before adding PrestoBlue reagent. After incubation for 20 min at 37 °C, the fluorescence was measured at an excitation of 535 nm (25 nm bandwidth) and an emission of 615 nm (10 nm bandwidth) using a microplate reader. The background fluorescence was measured at 615 nm as the blank well, and HepG2 cells cultured in FBS-free EMEM only were used as controls.

Molecular Dynamics Simulations. All of the simulations were performed with the NAMD code.[96] A time step of 1 fs was employed to integrate the equation of motions. A cutoff of 1.2 nm was used in conjunction with the particle mesh Ewald method to evaluate long-range Coulombic forces.[91] Bonded and nonbonded interactions were modeled by employing the various specifications of the CHARMM force field.[97,98] CharmmGUI was used to generate the initial configuration of the bilayer (symmetric, with POPC/cholesterol = 10), which was then equilibrated for a total time of 16 ns with a sequence of NVT, NPzAT (x and y coordinates are kept constant, while the z axis coordinates, corresponding to the normal to the bilayer, were allowed to vary). L-GQDs and D-GQDs (as single molecules or stacks) were placed less than 1 nm from the surface of the membrane, and the system was then minimized before the production runs. Production runs (45 and 25 ns for the single GQDs and the stacks, respectively) were performed in an NPsT ensemble, that is, an isothermal isobaric ensemble where only the changes of x and y axes are coupled.

ASSOCIATED CONTENT

Supporting Information

The Supporting Information is available free of charge on the ACS Publications website at DOI: 10.1021/acsnano.5b06369.

Additional methods, data, comments, and references (PDF)

AUTHOR INFORMATION

Corresponding Authors

*E-mail: avioli@umich.edu.

*E-mail: kotov@umich.edu.

Present Addresses

○(Jaewook Lee) Department of Mechanical and Manufacturing Engineering, University of Calgary, Calgary, Alberta T2N 1N4, Canada

□(Bongjun Yeom) Department of Chemical Engineering, Myongji University, Yongin 17058, Republic of Korea

Notes

The authors declare no competing financial interest.

ACKNOWLEDGMENTS

We are thankful to Mr. Ahmet Emre for TEM imaging of large commercial GQDs. We are also indebted to Prof. Liz-Marzan for stimulating discussions of SERS measurements. The central part of this work was supported by Center for Photonic and Multiscale Nanomaterials (C-PHOM) funded by the National Science Foundation (NSF) Materials Research Science and Engineering Center program DMR 1120923. Partial support of this work was also made by NSF projects 1403777, 1411014, 463474, JSPS KAKENHI Grant No. 2510001, and U.S. DOE BES Grant no. DE-SC0002619. The authors thank the University of Michigan's EMAL for its assistance with electron microscopy, and for the NSF Grant No. DMR-9871177 for funding of the JEOL 2010F analytical electron microscope used in this work.

REFERENCES

(1) Noguez, C.; Garzón, I. L. Optically Active Metal Nanoparticles. *Chem. Soc. Rev.* **2009**, *38*, 757−771.

(2) Knoppe, S.; Wong, O. A.; Malola, S.; Häkkinen, H.; Bürgi, T.; Verbiest, T.; Ackerson, C. J. Chiral Phase Transfer and Enantioenrichment of Thiolate-Protected Au_{102} Clusters. *J. Am. Chem. Soc.* **2014**, *136*, 4129−4132.

(3) Chen, W.; Bian, A.; Agarwal, A.; Liu, L.; Shen, H.; Wang, L.; Xu, C.; Kotov, N. A. Nanoparticle Superstructures Made by Polymerase Chain Reaction: Collective Interactions of Nanoparticles and a New Principle for Chiral Materials. *Nano Lett.* **2009**, *9*, 2153−2159.

(4) Govorov, A. O.; Gun'ko, Y. K.; Slocik, J. M.; Gérard, V. A.; Fan, Z.; Naik, R. R. Chiral Nanoparticle Assemblies: Circular Dichroism, Plasmonic Interactions, and Exciton Effects. *J. Mater. Chem.* **2011**, *21*, 16806.

(5) Kuzyk, A.; Schreiber, R.; Fan, Z.; Pardatscher, G.; Roller, E.-M.; Högele, A.; Simmel, F. C.; Govorov, A. O.; Liedl, T. DNA-Based Self-Assembly of Chiral Plasmonic Nanostructures with Tailored Optical Response. *Nature* **2012**, *483*, 311−314.

(6) Schaaff, T. G.; Whetten, R. L. Giant Gold−Glutathione Cluster Compounds: Intense Optical Activity in Metal-Based Transitions. *J. Phys. Chem. B* **2000**, *104*, 2630−2641.

(7) Yang, M.; Kotov, N. A. Nanoscale helices from inorganic materials. *J. Mater. Chem.* **2011**, *21*, 6775−6792.

(8) Moloney, M. P.; Gun'ko, Y. K.; Kelly, J. Chiral highly luminescent CdS quantum dots. *Chem. Commun.* **2007**, 3900−3902.

(9) Ma, W.; Kuang, H.; Xu, L.; Ding, L.; Xu, C.; Wang, L.; Kotov, N. A. Attomolar DNA Detection with Chiral Nanorod Assemblies. *Nat. Commun.* **2013**, *4*, 2689.

(10) Pendry, J. B. A Chiral Route to Negative Refraction. *Science* **2004**, *306*, 1353−1355.

(11) Kildishev, A. V.; Boltasseva, A.; Shalaev, V. M. Planar Photonics with Metasurfaces. *Science* **2013**, *339*, 1232009.

(12) Zhao, Y.; Xu, L.; Ma, W.; Wang, L.; Kuang, H.; Xu, C.; Kotov, N. A. Shell-Engineered Chiroplasmonic Assemblies of Nanoparticles for Zeptomolar DNA Detection. *Nano Lett.* **2014**, *14*, 3908−3913.

(13) Yasukawa, T.; Miyamura, H.; Kobayashi, S. Chiral Metal Nanoparticle-Catalyzed Asymmetric C-C Bond Formation Reactions. *Chem. Soc. Rev.* **2014**, *43*, 1450−1461.

(14) Xia, Y.; Zhou, Y.; Tang, Z. Chiral Inorganic Nanoparticles: Origin, Optical Properties and Bioapplications. *Nanoscale* **2011**, *3*, 1374−1382.

(15) Guerrero-Martínez, A.; Alonso-Gómez, J. L.; Auguié, B.; Cid, M. M.; Liz-Marzán, L. M. From Individual to Collective Chirality in Metal Nanoparticles. *Nano Today* **2011**, *6*, 381−400.

(16) Soukoulis, C. M.; Wegener, M. Past Achievements and Future Challenges in the Development of Three-Dimensional Photonic Metamaterials. *Nat. Photonics* **2011**, *5*, 523−530.

(17) Gansel, J. K.; Thiel, M.; Rill, M. S.; Decker, M.; Bade, K.; Saile, V.; von Freymann, G.; Linden, S.; Wegener, M. Gold Helix Photonic Metamaterial as Broadband Circular Polarizer. *Science* **2009**, *325*, 1513−1515.

(18) Moloney, M. P.; Govan, J.; Loudon, A.; Mukhina, M.; Gun'ko, Y. K. Preparation of Chiral Quantum Dots. *Nat. Protoc.* **2015**, *10*, 558−573.

(19) Nakashima, T.; Kobayashi, Y.; Kawai, T. Optical Activity and Chiral Memory of Thiol-Capped CdTe Nanocrystals. *J. Am. Chem. Soc.* **2009**, *131*, 10342−10343.

(20) Zhou, Y.; Zhu, Z.; Huang, W.; Liu, W.; Wu, S.; Liu, X.; Gao, Y.; Zhang, W.; Tang, Z. Optical Coupling between Chiral Biomolecules and Semiconductor Nanoparticles: Size-Dependent Circular Dichroism Absorption. *Angew. Chem., Int. Ed.* **2011**, *50*, 11456−11459.

DOI: 10.1021/acsnano.5b06369
ACS Nano 2016, 10, 1744−1755

(21) Yeom, J.; Yeom, B.; Chan, H.; Smith, K. W.; Dominguez-Medina, S.; Bahng, J. H.; Zhao, G.; Chang, W.-S.; Chang, S.-J.; Chuvilin, A.; Melnikau, D.; Rogach, A. L.; Zhang, P.; Link, S.; Král, P.; Kotov, N. A. Chiral Templating of Self-Assembling Nanostructures by Circularly Polarized Light. *Nat. Mater.* **2015**, *14*, 66−72.
(22) Geim, A. K.; Novoselov, K. S. The Rise of Graphene. *Nat. Mater.* **2007**, *6*, 183−191.
(23) Park, S.; Vosguerichian, M.; Bao, Z. A Review of Fabrication and Applications of Carbon Nanotube Film-Based Flexible Electronics. *Nanoscale* **2013**, *5*, 1727−1752.
(24) Eda, G.; Lin, Y.-Y.; Mattevi, C.; Yamaguchi, H.; Chen, H.-A.; Chen, I.-S.; Chen, C.-W.; Chhowalla, M. Blue Photoluminescence from Chemically Derived Graphene Oxide. *Adv. Mater.* **2010**, *22*, 505−509.
(25) Yavari, F.; Koratkar, N. Graphene-Based Chemical Sensors. *J. Phys. Chem. Lett.* **2012**, *3*, 1746−1753.
(26) Terrones, M. Science And Technology Of The Twenty -First Century: Synthesis, Properties, and Applications of Carbon Nanotubes. *Annu. Rev. Mater. Res.* **2003**, *33*, 419−501.
(27) Avouris, P.; Chen, Z.; Perebeinos, V. Carbon-Based Electronics. *Nat. Nanotechnol.* **2007**, *2*, 605−615.
(28) Maroto, E. E.; Izquierdo, M.; Reboredo, S.; Marco-Martínez, J.; Filippone, S.; Martín, N. Chiral Fullerenes from Asymmetric Catalysis. *Acc. Chem. Res.* **2014**, *47*, 2660−2670.
(29) Avouris, P.; Dimitrakopoulos, C. Graphene: Synthesis and Applications. *Mater. Today* **2012**, *15*, 86−97.
(30) Choi, W.; Lahiri, I.; Seelaboyina, R.; Kang, Y. S. *Synthesis of Graphene and Its Applications: A Review*; Taylor & Francis Group, 2010; Vol. *35*.
(31) Yang, F.; Wang, X.; Zhang, D.; Yang, J.; Luo, D.; Xu, Z.; Wei, J.; Wang, J.-Q.; Xu, Z.; Peng, F.; Li, X.; Li, R.; Li, Y.; Li, H.; Bai, X.; Ding, F.; Li, Y. Chirality-Specific Growth of Single-Walled Carbon Nanotubes on Solid Alloy Catalysts. *Nature* **2014**, *510*, 522−524.
(32) He, M.; Jiang, H.; Liu, B.; Fedotov, P. V.; Chernov, A. I.; Obraztsova, E. D.; Cavalca, F.; Wagner, J. B.; Hansen, T. W.; Anoshkin, I. V.; Obraztsova, E. A.; Belkin, A. V.; Sairanen, E.; Nasibulin, A. G.; Lehtonen, J.; Kauppinen, E. I. Chiral-Selective Growth of Single-Walled Carbon Nanotubes on Lattice-Mismatched Epitaxial Cobalt Nanoparticles. *Sci. Rep.* **2013**, *3*, 1460.
(33) Smith, D.; Woods, C.; Seddon, A.; Hoerber, H. Photophoretic Separation of Single-Walled Carbon Nanotubes: A Novel Approach to Selective Chiral Sorting. *Phys. Chem. Chem. Phys.* **2014**, *16*, 5221−5228.
(34) Liu, H.; Nishide, D.; Tanaka, T.; Kataura, H. Large-Scale Single-Chirality Separation of Single-Wall Carbon Nanotubes by Simple Gel Chromatography. *Nat. Commun.* **2011**, *2*, 309.
(35) Peng, X.; Komatsu, N.; Bhattacharya, S.; Shimawaki, T.; Aonuma, S.; Kimura, T.; Osuka, A. Optically Active Single-Walled Carbon Nanotubes. *Nat. Nanotechnol.* **2007**, *2*, 361−365.
(36) Ghosh, S.; Bachilo, S. M.; Weisman, R. B. Advanced Sorting of Single-Walled Carbon Nanotubes by Nonlinear Density-Gradient Ultracentrifugation. *Nat. Nanotechnol.* **2010**, *5*, 443−450.
(37) Tao, C.; Jiao, L.; Yazyev, O. V.; Chen, Y.-C.; Feng, J.; Zhang, X.; Capaz, R. B.; Tour, J. M.; Zettl, A.; Louie, S. G.; Dai, H.; Crommie, M. F. Spatially Resolving Edge States of Chiral Graphene Nanoribbons. *Nat. Phys.* **2011**, *7*, 616−620.
(38) Katsnelson, M. I.; Novoselov, K. S.; Geim, A. K. Chiral Tunnelling and the Klein Paradox in Graphene. *Nat. Phys.* **2006**, *2*, 620−625.
(39) Yokoyama, A.; Yoshida, M.; Ishii, A.; Kato, Y. K. Giant Circular Dichroism in Individual Carbon Nanotubes Induced by Extrinsic Chirality. *Phys. Rev. X* **2014**, *4*, 011005.
(40) Skandani, A. A.; Al-Haik, M. Reciprocal Effects of the Chirality and the Surface Functionalization on the Drug Delivery Permissibility of Carbon Nanotubes. *Soft Matter* **2013**, *9*, 11645−11649.
(41) Hong, G.; Diao, S.; Antaris, A. L.; Dai, H. Carbon Nanomaterials for Biological Imaging and Nanomedicinal Therapy. *Chem. Rev.* **2015**, *115*, 10816.
(42) Li, L.; Yan, X. Colloidal Graphene Quantum Dots. *J. Phys. Chem. Lett.* **2010**, *1*, 2572−2576.
(43) Chua, C. K.; Sofer, Z.; Šimek, P.; Jankovský, O.; Klímová, K.; Bakardjieva, S.; Hrdličková Kučková, Š.; Pumera, M. Synthesis of Strongly Fluorescent Graphene Quantum Dots by Cage-Opening Buckminsterfullerene. *ACS Nano* **2015**, *9*, 2548−2555.
(44) Bacon, M.; Bradley, S. J.; Nann, T. Graphene Quantum Dots. *Part. Part. Syst. Charact.* **2014**, *31*, 415−428.
(45) Trauzettel, B.; Bulaev, D. V.; Loss, D.; Burkard, G. Spin Qubits in Graphene Quantum Dots. *Nat. Phys.* **2007**, *3*, 192−196.
(46) Grigorenko, A. N.; Polini, M.; Novoselov, K. S. Graphene Plasmonics. *Nat. Photonics* **2012**, *6*, 749−758.
(47) Low, T.; Avouris, P. Graphene Plasmonics for Terahertz to Mid-Infrared Applications. *ACS Nano* **2014**, *8*, 1086−1101.
(48) Hu, T.; Isaacoff, B. P.; Bahng, J. H.; Hao, C.; Zhou, Y.; Zhu, J.; Li, X.; Wang, Z.; Liu, S.; Xu, C.; Biteen, J.; Kotov, N. A. Self-Organization of Plasmonic and Excitonic Nanoparticles into Resonant Chiral Supraparticle Assemblies. *Nano Lett.* **2014**, *14*, 6799−6810.
(49) Peng, J.; Gao, W.; Gupta, B. K.; Liu, Z.; Romero-Aburto, R.; Ge, L.; Song, L.; Alemany, L. B.; Zhan, X.; Gao, G.; Vithayathil, S. A.; Kaipparettu, B. A.; Marti, A.; Hayashi, T.; Zhu, J.-J.; Ajayan, P. Graphene Quantum Dots Derived from Carbon Fibers. *Nano Lett.* **2012**, *12*, 844−849.
(50) Choi, B. G.; Yang, M. H.; Park, T. J.; Huh, Y. S.; Lee, S. Y.; Hong, W. H.; Park, H. Programmable Peptide-Directed Two Dimensional Arrays of Various Nanoparticles on Graphene Sheets. *Nanoscale* **2011**, *3*, 3208−3213.
(51) Zhu, S.; Zhang, J.; Qiao, C.; Tang, S.; Li, Y.; Yuan, W.; Li, B.; Tian, L.; Liu, F.; Hu, R.; Gao, H.; Wei, H.; Zhang, H.; Sun, H.; Yang, B. Strongly Green-Photoluminescent Graphene Quantum Dots for Bioimaging Applications. *Chem. Commun.* **2011**, *47*, 6858−6860.
(52) Son, D. I.; Kwon, B. W.; Park, D. H.; Seo, W.-S.; Yi, Y.; Angadi, B.; Lee, C.-L.; Choi, W. K. Emissive ZnO-Graphene Quantum Dots for White-Light-Emitting Diodes. *Nat. Nanotechnol.* **2012**, *7*, 465−471.
(53) Diao, S.; Hong, G.; Robinson, J. T.; Jiao, L.; Antaris, A. L.; Wu, J. Z.; Choi, C. L.; Dai, H. Chirality Enriched (12,1) and (11,3) Single-Walled Carbon Nanotubes for Biological Imaging. *J. Am. Chem. Soc.* **2012**, *134*, 16971−16974.
(54) Mamedova, N. N.; Kotov, N. a.; Rogach, A. L.; Studer, J. Albumin−CdTe Nanoparticle Bioconjugates: Preparation, Structure, and Interunit Energy Transfer with Antenna Effect. *Nano Lett.* **2001**, *1*, 281−286.
(55) Franzl, T.; Koktysh, D. S.; Klar, T. A.; Rogach, A. L.; Feldmann, J.; Gaponik, N. Fast Energy Transfer in Layer-by-Layer Assembled CdTe Nanocrystal Bilayers. *Appl. Phys. Lett.* **2004**, *84*, 2904.
(56) Tavares, M. A. F. Excited Molecular Complexes of Aromatic Hydrocarbons. *Trans. Faraday Soc.* **1970**, *66*, 2431.
(57) Guo, H.-L.; Wang, X.-F.; Qian, Q.-Y.; Wang, F.-B.; Xia, X.-H. A Green Approach to the Synthesis of Graphene Nanosheets. *ACS Nano* **2009**, *3*, 2653−2659.
(58) Tuinstra, F. Raman Spectrum of Graphite. *J. Chem. Phys.* **1970**, *53*, 1126.
(59) Ferrari, A. C.; Meyer, J. C.; Scardaci, V.; Casiraghi, C.; Lazzeri, M.; Mauri, F.; Piscanec, S.; Jiang, D.; Novoselov, K. S.; Roth, S.; Geim, A. K. Raman Spectrum of Graphene and Graphene Layers. *Phys. Rev. Lett.* **2006**, *97*, 187401.
(60) Li, Y.; Hu, Y.; Zhao, Y.; Shi, G.; Deng, L.; Hou, Y.; Qu, L. An Electrochemical Avenue to Green-Luminescent Graphene Quantum Dots as Potential Electron-Acceptors for Photovoltaics. *Adv. Mater.* **2011**, *23*, 776−780.
(61) Kleinman, S. L.; Ringe, E.; Valley, N.; Wustholz, K. L.; Phillips, E.; Scheidt, K. A.; Schatz, G. C.; Van Duyne, R. P. Single-Molecule Surface-Enhanced Raman Spectroscopy of Crystal Violet Isotopologues: Theory and Experiment. *J. Am. Chem. Soc.* **2011**, *133*, 4115−4122.
(62) Sanz-Ortiz, M. N.; Sentosun, K.; Bals, S.; Liz-Marzán, L. M. Templated Growth of Surface Enhanced Raman Scattering-Active Branched Gold Nanoparticles within Radial Mesoporous Silica Shells. *ACS Nano* **2015**, *9*, 10489−10497.

DOI: 10.1021/acsnano.5b06369
ACS Nano 2016, 10, 1744−1755

(63) Cañamares, M. V.; Chenal, C.; Birke, R. L.; Lombardi, J. R. DFT, SERS, and Single-Molecule SERS of Crystal Violet. *J. Phys. Chem. C* **2008**, *112*, 20295−20300.
(64) Ye, J.; Shioi, M.; Lodewijks, K.; Lagae, L.; Kawamura, T.; Van Dorpe, P. Tuning Plasmonic Interaction between Gold Nanorings and a Gold Film for Surface Enhanced Raman Scattering. *Appl. Phys. Lett.* **2010**, *97*, 163106.
(65) Paik, M.-J.; Kang, J. S.; Huang, B.-S.; Carey, J. R.; Lee, W. Development and Application of Chiral Crown Ethers as Selectors for Chiral Separation in High-Performance Liquid Chromatography and Nuclear Magnetic Resonance Spectroscopy. *J. Chromatogr. A* **2013**, *1274*, 1−5.
(66) Chen, Z.; Wang, Q.; Wu, X.; Li, Z.; Jiang, Y.-B. Optical Chirality Sensing Using Macrocycles, Synthetic and Supramolecular Oligomers/polymers, and Nanoparticle Based Sensors. *Chem. Soc. Rev.* **2015**, *44*, 4249.
(67) Barberá, J.; Puig, L.; Romero, P.; Serrano, J. L.; Sierra, T. Supramolecular Helical Mesomorphic Polymers. Chiral Induction through H-Bonding. *J. Am. Chem. Soc.* **2005**, *127*, 458−464.
(68) Zhu, Z.; Liu, W.; Li, Z.; Han, B.; Zhou, Y.; Gao, Y.; Tang, Z. Manipulation of Collective Optical Activity in One-Dimensional Plasmonic Assembly. *ACS Nano* **2012**, *6*, 2326−2332.
(69) Yeom, B.; Zhang, H.; Zhang, H.; Park, J. I.; Kim, K.; Govorov, A. O.; Kotov, N. A. Chiral Plasmonic Nanostructures on Achiral Nanopillars. *Nano Lett.* **2013**, *13*, 5277−5283.
(70) Zhou, Y.; Yang, M.; Sun, K.; Tang, Z.; Kotov, N. A. Similar Topological Origin of Chiral Centers in Organic and Nanoscale Inorganic Structures: Effect of Stabilizer Chirality on Optical Isomerism and Growth of CdTe Nanocrystals. *J. Am. Chem. Soc.* **2010**, *132*, 6006−6013.
(71) Liu, H.; Ye, Y.; Chen, J.; Lin, D.; Jiang, Z.; Liu, Z.; Sun, B.; Yang, L.; Liu, J. In Situ Photoreduced Silver Nanoparticles on Cysteine: An Insight into the Origin of Chirality. *Chem. - Eur. J.* **2012**, *18*, 8037−8041.
(72) Wu, X.; Xu, L.; Liu, L.; Ma, W.; Yin, H.; Kuang, H.; Wang, L.; Xu, C.; Kotov, N. A. Unexpected Chirality of Nanoparticle Dimers and Ultrasensitive Chiroplasmonic Bioanalysis. *J. Am. Chem. Soc.* **2013**, *135*, 18629−18636.
(73) Peterca, M.; Imam, M. R.; Ahn, C.-H.; Balagurusamy, V. S. K.; Wilson, D. A.; Rosen, B. M.; Percec, V. Transfer, Amplification, and Inversion of Helical Chirality Mediated by Concerted Interactions of C3-Supramolecular Dendrimers. *J. Am. Chem. Soc.* **2011**, *133*, 2311−2328.
(74) Al-Jamal, K. T.; Ramaswamy, C.; Florence, A. T. Supramolecular Structures from Dendrons and Dendrimers. *Adv. Drug Delivery Rev.* **2005**, *57*, 2238−2270.
(75) Liu, M.; Zhang, L.; Wang, T. Supramolecular Chirality in Self-Assembled Systems. *Chem. Rev.* **2015**, *115*, 7304−7397.
(76) Yan, W.; Xu, L.; Xu, C.; Ma, W.; Kuang, H.; Wang, L.; Kotov, N. A. Self-Assembly of Chiral Nanoparticle Pyramids with Strong R/S Optical Activity. *J. Am. Chem. Soc.* **2012**, *134*, 15114−15121.
(77) Lu, Q.; Arroyo, M.; Huang, R. Elastic Bending Modulus of Monolayer Graphene. *J. Phys. D: Appl. Phys.* **2009**, *42*, 102002.
(78) Efrati, E.; Klein, Y.; Aharoni, H.; Sharon, E. Spontaneous Buckling of Elastic Sheets with a Prescribed Non-Euclidean Metric. *Phys. D* **2007**, *235*, 29−32.
(79) Sharon, E.; Roman, B.; Marder, M.; Shin, G.-S.; Swinney, H. L. Mechanics. Buckling Cascades in Free Sheets. *Nature* **2002**, *419*, 579.
(80) Kwasniewski, S. P.; Deleuze, M. S.; Francois, J. P. Optical Properties of Trans-Stilbene Using Semiempirical and Time-Dependent Density Functional Theory: A Comparative Study. *Int. J. Quantum Chem.* **2000**, *80*, 672−680.
(81) Miyashita, A.; Yasuda, A.; Takaya, H.; Toriumi, K.; Ito, T.; Souchi, T.; Noyori, R. Synthesis of 2,2′-Bis(diphenylphosphino)-1,1′-Binaphthyl (BINAP), an Atropisomeric Chiral Bis(triaryl)phosphine, and Its Use in the rhodium(I)-Catalyzed Asymmetric Hydrogenation of.alpha.-(acylamino)acrylic Acids. *J. Am. Chem. Soc.* **1980**, *102*, 7932−7934.
(82) Ma, W.; Kuang, H.; Wang, L.; Xu, L.; Chang, W.-S.; Zhang, H.; Sun, M.; Zhu, Y.; Zhao, Y.; Liu, L.; Xu, C.; Link, S.; Kotov, N. A. Chiral Plasmonics of Self-Assembled Nanorod Dimers. *Sci. Rep.* **2013**, *3*, 1934.
(83) Auguié, B.; Alonso-Gómez, J. L.; Guerrero-Martínez, A.; Liz-Marzán, L. M. Fingers Crossed: Optical Activity of a Chiral Dimer of Plasmonic Nanorods. *J. Phys. Chem. Lett.* **2011**, *2*, 846−851.
(84) Li, Y.; Zhou, Y.; Wang, H.-Y.; Perrett, S.; Zhao, Y.; Tang, Z.; Nie, G. Chirality of Glutathione Surface Coating Affects the Cytotoxicity of Quantum Dots. *Angew. Chem., Int. Ed.* **2011**, *50*, 5860−5864.
(85) Smith, S. W. Chiral Toxicology: It's the Same Thing···only Different. *Toxicol. Sci.* **2009**, *110*, 4−30.
(86) Reddy, I. K.; Kommuru, T. R.; Zaghloul, A. A.; Khan, M. A. Chirality and Its Implications in Transdermal Drug Development. *Crit. Rev. Ther. Drug Carrier Syst.* **2000**, *17*, 285−325.
(87) Nguyen, L. A.; He, H.; Pham-Huy, C. Chiral Drugs: An Overview. *Int. J. Biomed. Sci.* **2006**, *2*, 85−100.
(88) Baranes, K.; Moshe, H.; Alon, N.; Schwartz, S.; Shefi, O. Neuronal Growth on L- and D-Cysteine Self-Assembled Monolayers Reveals Neuronal Chiral Sensitivity. *ACS Chem. Neurosci.* **2014**, *5*, 370−376.
(89) Yao, X.; Hu, Y.; Cao, B.; Peng, R.; Ding, J. Effects of Surface Molecular Chirality on Adhesion and Differentiation of Stem Cells. *Biomaterials* **2013**, *34*, 9001−9009.
(90) Silvera Batista, C. A.; Larson, R. G.; Kotov, N. A. Nonadditivity of Nanoparticle Interactions. *Science* **2015**, *350*, 1242477−1242477.
(91) Darden, T.; York, D.; Pedersen, L. Particle Mesh Ewald: An N·log(N) Method for Ewald Sums in Large Systems. *J. Chem. Phys.* **1993**, *98*, 10089.
(92) Brooks, B. R.; Brooks, C. L.; MacKerell, A. D.; Nilsson, L.; Petrella, R. J.; Roux, B.; Won, Y.; Archontis, G.; Bartels, C.; Boresch, S.; Caflisch, A.; Caves, L.; Cui, Q.; Dinner, A. R.; Feig, M.; Fischer, S.; Gao, J.; Hodoscek, M.; Im, W.; Kuczera, K.; et al. CHARMM: The Biomolecular Simulation Program. *J. Comput. Chem.* **2009**, *30*, 1545−1614.
(93) Ye, R.; Xiang, C.; Lin, J.; Peng, Z.; Huang, K.; Yan, Z.; Cook, N. P.; Samuel, E. L. G.; Hwang, C.-C.; Ruan, G.; Ceriotti, G.; Raji, A. R. O.; Martí, A. A.; Tour, J. M. Coal as an Abundant Source of Graphene Quantum Dots. *Nat. Commun.* **2013**, *4*, 2943.
(94) Tohgha, U.; Deol, K. K.; Porter, A. G.; Bartko, S. G.; Choi, J. K.; Leonard, B. M.; Varga, K.; Kubelka, J.; Muller, G.; Balaz, M. Ligand Induced Circular Dichroism and Circularly Polarized Luminescence in CdSe Quantum Dots. *ACS Nano* **2013**, *7*, 11094−11102.
(95) Brocki, T.; Moskovits, M.; Bosnich, B. Vibrational Optical Activity. Circular Differential Raman Scattering from a Series of Chiral Terpenes. *J. Am. Chem. Soc.* **1980**, *102*, 495−500.
(96) Phillips, J. C.; Braun, R.; Wang, W.; Gumbart, J.; Tajkhorshid, E.; Villa, E.; Chipot, C.; Skeel, R. D.; Kalé, L.; Schulten, K. Scalable Molecular Dynamics with NAMD. *J. Comput. Chem.* **2005**, *26*, 1781−1802.
(97) Vanommeslaeghe, K.; Hatcher, E.; Acharya, C.; Kundu, S.; Zhong, S.; Shim, J.; Darian, E.; Guvench, O.; Lopes, P.; Vorobyov, I.; Mackerell, A. D., Jr. CHARMM General Force Field: A Force Field for Drug-like Molecules Compatible with the CHARMM All-Atom Additive Biological Force Fields. *J. Comput. Chem.* **2010**, *31*, 671−690.
(98) Klauda, J. B.; Venable, R. M.; Freites, J. A.; O'Connor, J. W.; Tobias, D. J.; Mondragon-Ramirez, C.; Vorobyov, I.; MacKerell, A. D.; Pastor, R. W. Update of the CHARMM All-Atom Additive Force Field for Lipids: Validation on Six Lipid Types. *J. Phys. Chem. B* **2010**, *114*, 7830−7843.

DOI: 10.1021/acsnano.5b06369
ACS Nano 2016, 10, 1744−1755